

Journal Pre-proof

Deterministic relation between thermal-phonon dressings and non-Hermitian multi-Fano interferences router in ion-doped microcrystals

Huanrong Fan, Faizan Raza, Anas Mujahid, Peng Li, Yafen Wang, Haitian Tang, Muhammad Usman, Bo Li, Changbiao Li, Yanpeng Zhang



PII: S2709-4723(23)00040-0

DOI: <https://doi.org/10.1016/j.chip.2023.100077>

Reference: CHIP 100077

To appear in: *Chip*

Received Date: 4 September 2023

Revised Date: 30 October 2023

Accepted Date: 24 November 2023

Please cite this article as: Fan H, Raza F, Mujahid A, Li P, Wang Y, Tang H, Usman M, Li B, Li C, Zhang Y, Deterministic relation between thermal-phonon dressings and non-Hermitian multi-Fano interferences router in ion-doped microcrystals, *Chip*, <https://doi.org/10.1016/j.chip.2023.100077>.

This is a PDF file of an article that has undergone enhancements after acceptance, such as the addition of a cover page and metadata, and formatting for readability, but it is not yet the definitive version of record. This version will undergo additional copyediting, typesetting and review before it is published in its final form, but we are providing this version to give early visibility of the article. Please note that, during the production process, errors may be discovered which could affect the content, and all legal disclaimers that apply to the journal pertain.

© 2023 The Author(s). Published by Elsevier B.V. on behalf of Shanghai Jiao Tong University.

Deterministic relation between thermal-phonon dressings and non-Hermitian multi-Fano interferences router in ion-doped microcrystals

Huanrong Fan^{1, #}, Faizan Raza^{1, #}, Anas Mujahid^{1, #}, Peng Li², Yafen Wang¹, Haitian Tang¹, Muhammad Usman¹, Bo Li^{1, §}, Changbiao Li^{1, †} and Yanpeng Zhang^{1, *}

¹Key Laboratory for Physical Electronics and Devices of the Ministry of Education & Shaanxi Key Lab of Information Photonic Technique, Xi'an Jiaotong University, Xi'an 710049, China

²Center for Regenerative and Reconstructive Medicine, Med-X Institute, the First Affiliated Hospital of Xi'an Jiaotong University, Xi'an 710061, China

[#]These authors contributed equally to this work.

*e-mail: ypzhang@mail.xjtu.edu.cn

[†]e-mail: cbli@mail.xjtu.edu.cn

[§]e-mail: libophy@xjtu.edu.cn

We report the multi-Fano interference obtained through the simultaneous acquisition of bright and dark states in different phase transitions of Eu^{3+} : BiPO_4 (7:1, 6:1, 1:1, and 0.5:1) and Eu^{3+} : NaYF_4 (1:1/4) crystals. We employ multi-dressed spontaneous four-wave mixing and multi-dressed fluorescence (multi-order) to optimize the strong photon-phonon nested dressing

effect resulting in more obvious multi-Fano interference. Firstly, the multi-Fano is produced through interference in continuous and multi-bound states. Secondly, five multi-Fano dips originate from nested five dressings (one photon and four phonons) under symmetrical splitting of $^7\text{F}_1$ energy level. We depict that the pure H-phase (0.5:1) sample exhibits the strongest photon-phonon dressed effect (five Fano dips). Further, we investigate high-order non-Hermitian exceptional points in multi-Fano interference by adjusting the ratio of Rabi-frequency to de-phase rate through nested photon and phonon dressing. Our experimental results are validated by theoretical simulations, which may be applied to designing optoelectronic devices such as non-Hermitian multi-Fano interferences (multi-channel) router.

Keywords: Multi-Fano interferences, Thermal-phonon dressings, Non-Hermitian, Router

INTRODUCTION

In recent times, there has been a notable surge in research efforts on Fano resonance, primarily driven by its extensive range of material applications within the realms of physical, chemical, and biological sciences.¹⁻⁷ There is significant potential for the application of structures with Fano resonance that we can expect in the field of hybrid photonics and nanophotonics related to the coupling of light with various particles and quasi-particles such as phonons, electrons, spins, excitons, and mechanical degrees of freedom⁸. In Fano interference, interference of a discrete quantum state with a continuum of states sharing the same energy leads to the appearance of asymmetric line shapes in the measured excitation spectra, which can be characterized by

a Fano 'shape' parameter, which was first observed in experiments exciting rare gas atoms to Rydberg states^{9,10}. Fano lineshapes serve as essential spectroscopic indicators that provide quantitatively insights into the structural and dynamic properties of physical objects, spanning from nuclei to three-dimensional solids and liquids.

In recent studies, there has been a special emphasis on exploring higher-order Exceptional points (EP)¹¹⁻¹³ and Parity Time (PT) symmetric systems that involve alternating Gain and Loss¹⁴⁻¹⁸. These systems have shown potential for effectively controlling non-Hermitian multi-Fano interference. The applications of Fano resonance encompass various domains, including the utilization of linear and nonlinear dielectric nano resonators, 2D materials¹⁹⁻²¹, slow light optomechanical nanocavities²², Dirac

semiconductors with ultrafast dynamics of phase and topology²³, Fano-lasers and spacers^{24,25}, Fano devices^{26,27}. Being so sensitive to changes in geometry and surroundings, Fano-based devices provide major implementation hurdles despite being an essential component of effective sensors.

In a bid to address this challenge, there has been significant recognition of the merits of exploiting rare-earth ion-doped crystals for the advancement of integrated quantum circuits. The lifetime, coherence time, and spectral resolution of doped crystals such as Eu^{3+} : YPO_4 , Pr^{3+} : Y_2SiO_5 , and Eu^{3+} : BiPO_4 can be precisely controlled through the nonlinear process^{28,29}. But, among them Eu^{3+} : BiPO_4 is the best candidate due to the longest coherence among other doped crystals owing to photon-phonon dressing³⁰⁻³³. The functional crystal of BiPO_4 has three different crystal structures, namely, hexagonal phase (HP, space group: $\text{P}6_3\text{121}$), low-temperature monoclinic phase (LTMP, space group: $\text{P}2_1/\text{n}$), and high-temperature monoclinic phase (HTMP, space group: $\text{P}2_1/\text{m}$)^{34,35}. The phase transition of BiPO_4 from LTMP or HTMP to HP occurs by continuously doping Ln^{3+} ions. Our research investigates the effective manipulation of the phase transition, which results in the identification of the novel phenomena of multi-Fano resonances controlled through photon-phonon interaction and multi-dressing effect. However, all of the spectral Fano interferences that have been previously reported involved a single Fano interference arising from the interaction between one continuous state and one bound state, solely caused by external photon dressing.

In this paper, we report the complex relationship between novel multi-Fano interference and phase transitions of ion-doped microcrystals (Eu^{3+} : $\text{BiPO}_4/\text{Eu}^{3+}$: NaYF_4). Our results show that each BiPO_4 fine structure energy level exhibits distinct lattice vibrations, which result in different phonon frequencies. As

a consequence, the number of dressing levels varies, leading to the observation of multi-Fano interferences. The evolution of five Fano interferences from a single Fano interference was observed by precisely controlling the interaction between a continuous state and multi-bound states using laser power, temperature, and gate position (GP). In our experiment, single laser excitation results in a single Fano dip caused by the self-dressing effect, whereas multi-dressing is generated from photon-phonon multi-Fano interference. We realize the non-Hermitian controlled higher-order exceptional points (EPs), which can be defined by real and imaginary quantization alignment. We apply our outcomes to suggest a non-Hermitian multi-channel router and show that broadband peak input fluorescence (FL) to multi-Fano output can be achieved. This study explores extensively into the correlation between thermal-phonon dressings and multi-Fano interference in ion-doped microcrystals, with potential applications in the development of optoelectronic devices.

EXPERIMENTAL SETUP

In our experiment the molar ratio (PO_4^{3-} : [Bi^{3+} + Eu^{3+}]) of doped ions is adjusted with different concentrations of Hexagonal- (H) and monoclinic (M) phase to obtain different phase transitions of BiPO_4 nanocrystals (7:1, 6:1, 1:1, 0.5:1) as shown in Fig. S1(a-f) (See Supply Information for detailed physical images of the samples). The (7:1, 6:1, 1:1) BiPO_4 crystals with C_1 point group site-symmetry has a proportion of M-phase whereas the concentration of H-phase is high in (0.5:1) BiPO_4 sample (C_2 symmetry) resulting in more lattice vibrating phonon^{36,37}. The Eu^{3+} : NaYF_4 (YF_4^{3-} : [Na^{3+} + Eu^{3+}] = 1:1/4) has pure H-phase with Cs symmetry. The transition between H-phase to M-phase has been achieved by increasing the phosphate ion (PO_4^{3-}) concentration in the Eu^{3+} : BiPO_4 system while

different crystal phases are synthesized by adjusting the pH values³⁸⁻⁴².

In our experiment, samples were held in a cryostat (CFM-102) with temperatures varying from 300K (strong phonon dressing) to 77K (weak phonon dressing) by flowing liquid nitrogen. Figures 1a1 and 1a2 show crystal field (CF) splitting levels of $\text{Eu}^{3+}:\text{BPO}_4$ and $\text{Eu}^{3+}:\text{NaYF}_4$, respectively. Figure 1a3 shows photon-assisted crystal field splitting in $\text{Eu}^{3+}:\text{BPO}_4/\text{NaYF}_4$. The ${}^7\text{F}_1$ fine structure ($J = 1$) splits into three levels ${}^7\text{F}_{1, \text{MJ}=-1}$ (587.3nm), ${}^7\text{F}_{1, \text{MJ}=0}$ (592.3nm), and ${}^7\text{F}_{1, \text{MJ}=+1}$ (597.3nm) under the dressing and crystal field effect of BiPO_4 . Figure 1b illustrates the sub-energy levels that corresponds to Figure 1a3. Two dye lasers (narrow scan with a 0.04 cm^{-1} linewidth and broad scan with a 0.08 cm^{-1} linewidth, R610 dye) pumped by an injection-locked single-mode Nd: YAG laser (Continuum Powerlite DLS 9010, 10Hz repetition rate, 5ns pulse width) were used to generate the two pumping fields $E_1 (\omega_1)$ and $E_2 (\omega_2)$. By exciting $\text{Eu}^{3+}:\text{BiPO}_4$ crystal with E_1 and E'_1 (reflection of E_1) (Fig. 1d), the output Stokes (E_s)/anti-Stokes (E_{As}) signals are generated under phase-matched condition ($k'_1 + k_1 = k_s + k_{As}$) due to interaction with $\text{Eu}^{3+}:\text{BiPO}_4$ energy levels. The out-of-phase FL1 and FL2 are generated through E_1 (broadband laser) and E_2 (narrowband laser), respectively. The pulse generated from Nd³⁺: YAG laser is used to simultaneously trigger a boxcar gated integrator (G) and oscilloscope (OS). The input laser beams are along the [010] axis of the crystal, which is perpendicular to the optical axis. The

spectral optical outputs are obtained by scanning laser frequency, while the time-resolved OS obtains temporal optical outputs by fixing DL frequency. The grating motor of DL1 and DL2 is scanned by computer to form the x-axis (wavelength), and the intensity of the excitation spectrum is the average of ten shots from the gated integrator appearing on the y-axis. The optical signal generated is detected at photomultiplier tubes (PMT) via confocal lenses (CL) in Fig. S1(g) (See Supply Information for detailed experimental setup). While PMT2 is positioned close to the sample to detect hybrid signal ($\text{FL} + E_{s/As}$) with dominant FL emission, PMT1 (near detector position) and PMT3 (far detector position) are precisely positioned to detect the generated in-phase spontaneous four-wave mixing (SFWM) (Fig. 1b). By adjusting the gate position, one can obtain output signals from different energy levels with different lifetimes. The ratio of FL to $E_{s/As}$ in a hybrid signal is controlled by gate position. Due to the distinct decay rates exhibited by the FL and SFWM, they can be easily differentiated at the PMT by employing a boxcar gate position. Furthermore, Fano resonance strongly depends upon point group site symmetry of different phases of $\text{Eu}^{3+}:\text{BiPO}_4$. Figure 1c shows the proposed model of a non-Hermitian multi-channel optical router. Figure 1d shows the dressing-like-Zeeman splitting of ${}^7\text{F}_1$ energy level. For the ${}^7\text{F}_1$ energy level by dressing field quantized rotation, we can get splitting energy levels ${}^7\text{F}_{1, \text{MJ}=-1}$, ${}^7\text{F}_{1, \text{MJ}=0}$, and ${}^7\text{F}_{1, \text{MJ}=+1}$.

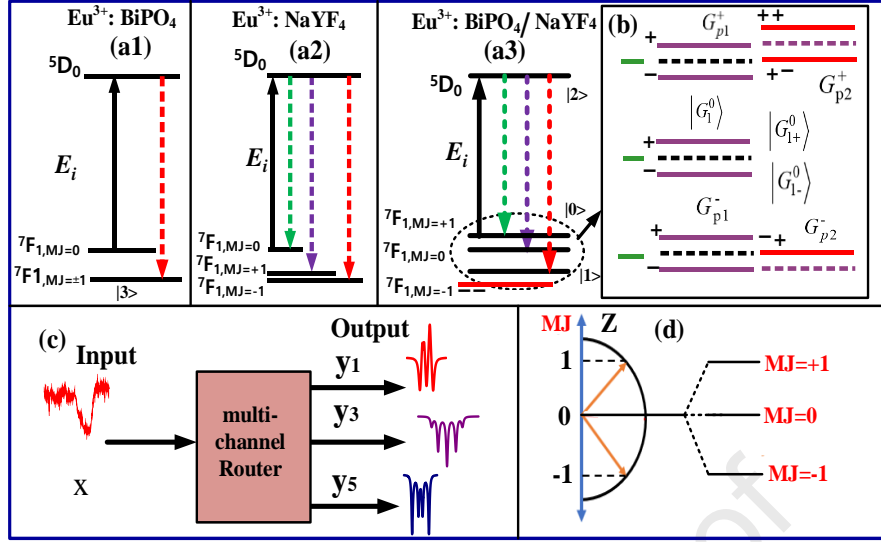


Fig. 1 **a1** and **a2** Crystal field splitting of 7F_1 energy level for Eu^{3+} : BiPO_4 and Eu^{3+} : NaYF_4 , respectively. **a3** Photon assistance crystal field splitting in Eu^{3+} : $\text{BiPO}_4/\text{NaYF}_4$. **b** Enlarged view of 7F_1 energy levels corresponding to **a**. **c** Model of a non-Hermitian multi-channel router. **d** Dressing like-Zeeman splitting (7F_1 , $MJ=\pm 1$, 7F_1 , $MJ=0$ and 7F_1 , $MJ=\pm 1$) in Eu^{3+} : BiPO_4 .

THEORETICAL MODEL

Our proposed model shows that more phonons can couple more energy levels as shown in Fig. 1a3. The excitation from single- and two-lasers shows single Fano dip (self-dressing) and multi-Fano dips (external dressing), respectively. It is worth mentioning that multi-dressing can only be generated from photon-phonon multi-Fano interference, not through one or two lasers' excitations. For Eu^{3+} : BiPO_4 sample, unique lattice vibrations can produce phonons with different frequencies which are coupled to different crystal field splitting levels ${}^5D_1 \rightarrow {}^7F_1$, ${}^5D_0 \rightarrow {}^7F_1$ and ${}^5D_0 \rightarrow {}^7F_3$ in the ion Eu^{3+} .

Therefore, more phonon results in effective dressing³⁶. Our findings reveal the five sharp dips which can only be explained by the combined effect of photon dressing and phonon.

A. The non-Hermitian multi-Fano of one laser

By opening field E_1 , the dressed third-order density matrix element for E_S ($\rho_S^{(3)}$) and E_{AS} ($\rho_{AS}^{(3)}$) via perturbation chains

$$\rho_{00}^{(0)} \xrightarrow{E_1} \rho_{20}^{(1)} \xrightarrow{E_{AS}} \rho_{00}^{(2)} \xrightarrow{E_1} \rho_{20(S)}^{(3)} \quad \text{and}$$

$$\rho_{00}^{(0)} \xrightarrow{E_1} \rho_{20}^{(1)} \xrightarrow{E_S} \rho_{00}^{(2)} \xrightarrow{E_1} \rho_{20(AS)}^{(3)}, \quad \text{respectively can be}$$

written as

$$\rho_{S(2)}^{(3)} = \frac{-iG_1 G_{AS} G_1'}{(\Gamma_{20} + i\Delta_1)(\Gamma_{00} + i\Delta_1 - i\Delta_{AS} + d_1)(\Gamma_{20} + \Delta_1 - i\Delta_{AS} + i\Delta_1')} = \rho_{S(2)}^{(3)} + \rho_{S(2)}^{(5)} + \rho_{S(2)}^{(7)}, \quad (1)$$

$$\rho_{AS(2)}^{(3)} = \frac{-iG_1 G_S G_1'}{(\Gamma_{20} + i\Delta_1)(\Gamma_{00} + i\Delta_1' - i\Delta_S + d_2)(\Gamma_{20} + i\Delta_1' - i\Delta_S + i\Delta_1)} = \rho_{AS(2)}^{(3)} + \rho_{AS(2)}^{(5)} + \rho_{AS(2)}^{(7)}, \quad (2)$$

Where $d_1 = |G_1|^2 / (\Gamma_{20} + i\Delta_1 - i\Delta_{AS} + d_3)$, $d_3 = |G_{p1}|^2 / (\Gamma_{10} + i\Delta_1 - i\Delta_{AS} - i\Delta_{p1})$,

$$d_2 = |G_1|^2 / (\Gamma_{20} + i\Delta_1' - i\Delta_S + d_4), \quad d_4 = |G_{p1}|^2 / (\Gamma_{10} + i\Delta_1' - i\Delta_S - i\Delta_{p1}),$$

$|\rho_{S/AS}^{(3)}| = (A^2 + B^2 + C^2 + 2AB\cos(\Delta\phi_1) + 2AC\cos(\Delta\phi_2) + 2BC\cos(\Delta\phi_3))^{1/2}$. The linewidth

of the $E_{S/AS}$ signal is $\Gamma_{S/AS} = \Gamma_{20} + \Gamma_{00} + \Gamma_{20}$. The

transverse de-phase rate $\Gamma_{ij} = (\Gamma_i + \Gamma_j)/2$,

$$\Gamma_{ij} = \Gamma_{pop} + \Gamma_{ion-spin} + \Gamma_{ion-ion} + \Gamma_{phonon} - \Gamma_{dressing}, \quad \text{where}$$

Γ_{phonon} is related to the sample temperature and

$\Gamma_{dressing}$ is associated with dressing. Here, two

Fano interferences are controlled by three phases ($\Delta\phi_1 = \pi$, $\Delta\phi_2 = \pi$, $\Delta\phi_3 = 0$). The above

equations show nested double dressing suggesting two-Fano interference originates from one continuous state $\rho_{S/AS}^{(3)}$ and two bound states (photon1 $\rho_{S/AS}^{(5)}$ photon1-phonon1 $\rho_{S/AS}^{(7)}$). $G_i = -\mu_H H / \hbar$ is the photon Rabi frequency, where H is the magnetic field for Rabi frequency, μ_H is the magnetic dipole matrix elements levels $|m\rangle$ and $|n\rangle$ and $|m\rangle$ and $|n\rangle$ are the crystal field splitting energy levels of 5D_0 and 7F_1 , respectively. Γ_{mn} is the transverse decay rate between levels $|m\rangle$ and $|n\rangle$. The frequency detuning $\Delta_i = \Omega_{mn} - \omega_i$, where Ω_{kl} is the corresponding atomic transition frequency between levels $|m\rangle$ and $|n\rangle$. ω_i is the frequency of the laser field E_i .

Photon excitation results from the interaction of laser light with the host material (Eu³⁺: BiPO₄). On the other hand, phonon

excitation arises from the interaction of the doped ion with a source of phonons (crystal lattice vibration), which are vibrations in the crystal lattice. The phonon Rabi frequency is described as the phonon Rabi frequency $G_{pi} = -\mu_{kl} E_{pi} / \hbar$, μ_{kl} which is the dipole moment between $|k\rangle$ and $|l\rangle$ of crystal field energy levels in 7F_1 . ω_{pi} is the phonon frequency of phonon field E_{pi} , which is determined by the vibration frequency of crystal lattice state mode. The Γ_{kl} is the transverse decay rate between $|k\rangle$ and $|l\rangle$. $G_i = -\mu_{kl} E_i / \hbar$ is the frequency detuning, where Ω_{kl} is the resonant frequency between $|k\rangle$ and $|l\rangle$. ω_i is the frequency of photon field E_i , which is determined by the vibration frequency of crystal lattice state mode. For the three dark states of nested three dressing, the expression (figure 5e) can be written as

$$\rho_{S(3)}^{(3)} = \frac{-iG_i G_{AS} G'_i}{(\Gamma_{20} + i\Delta_1 + d_{00})(\Gamma_{00} + i\Delta_1 - i\Delta_{AS})(\Gamma_{20} + i\Delta_1 + i\Delta'_1 - i\Delta_{AS}))} = \rho_{S(3)}^{(3)} + \rho_{S(3)}^{(5)} + \rho_{S(3)}^{(7)} + \rho_{S(3)}^{(9)}, \quad (3)$$

$$\rho_{AS(3)}^{(3)} = \frac{-iG_i G_s G'_i}{(\Gamma_{20} + i\Delta'_1 + d'_{00})(\Gamma_{00} + i\Delta'_1 - i\Delta_s)(\Gamma_{20} + i\Delta'_1 + i\Delta_1 - i\Delta_s)} = \rho_{AS(3)}^{(3)} + \rho_{AS(3)}^{(5)} + \rho_{AS(3)}^{(7)} + \rho_{AS(3)}^{(9)}, \quad (4)$$

where, $d_{00} = |G_1|^2 / (\Gamma_{20} + i\Delta_1 + |G_{p1}|^2 / (\Gamma_{10} + i\Delta_1 - i\Delta_{p1} + |G_{p2}|^2 / (\Gamma_{13} + i\Delta_1 - i\Delta_{p1} - i\Delta_{p2})))$,

$$d'_{00} = |G_1|^2 / (\Gamma_{20} + i\Delta'_1 + |G_{p1}|^2 / (\Gamma_{10} + i\Delta'_1 - i\Delta_{p1} + |G_{p2}|^2 / (\Gamma_{13} + i\Delta'_1 - i\Delta_{p1} - i\Delta_{p2})))$$

$$|\rho_{S/AS}^{(3)} + \rho_{S/AS}^{(5)} + \rho_{S/AS}^{(7)} + \rho_{S/AS}^{(9)}| = (A^2 + B^2 + C^2 + D^2 + 2AB\cos(\Delta\varphi_1) + 2AC\cos(\Delta\varphi_2) + 2AD\cos(\Delta\varphi_3) + 2BC\cos(\Delta\varphi_4) + 2BD\cos(\Delta\varphi_5) + 2CD\cos(\Delta\varphi_6))^{1/2}$$

Equations (3-4) represent nested three dressing

resulting in three-Fano interference, which originates from an imperfect continuous state ($\rho_{S/AS}^{(3)}$) and three bound (photon1 $\rho_{S/AS}^{(5)}$ photon1-phonon1 $\rho_{S/AS}^{(7)}$ photon1-phonon1-phonon2 $\rho_{S/AS}^{(9)}$) states. The three Fano interferences are governed by six phases ($\Delta\varphi_1 = \pi$, $\Delta\varphi_2 = \pi$, $\Delta\varphi_3 = \pi$, $\Delta\varphi_4 = 0$, $\Delta\varphi_5 = 0$, $\Delta\varphi_6 = 0$). For the four dark states of nested four dressing, the expression can be written as

$$\rho_{S(4)}^{(3)} = \frac{-iG_i G_{AS} G'_i}{(\Gamma_{20} + i\Delta_1 + d_3)(\Gamma_{00} + i\Delta_1 - i\Delta_s)(\Gamma_{20} + i\Delta_1 + i\Delta'_1 - i\Delta_s))} = \rho_{S(4)}^{(3)} + \rho_{S(4)}^{(5)} + \rho_{S(4)}^{(7)} + \rho_{S(4)}^{(9)} + \rho_{S(4)}^{(11)}, \quad (5)$$

$$\rho_{AS(4)}^{(3)} = \frac{-iG_i G_s G'_i}{(\Gamma_{20} + i\Delta_1 + d_4)(\Gamma_{00} + i\Delta_1 - i\Delta_s)(\Gamma_{20} + i\Delta_1 + i\Delta'_1 - i\Delta_s))} = \rho_{AS(4)}^{(3)} + \rho_{AS(4)}^{(5)} + \rho_{AS(4)}^{(7)} + \rho_{AS(4)}^{(9)} + \rho_{AS(4)}^{(11)}. \quad (6)$$

where $d_3 = |G_1|^2 / (\Gamma_{20} + i\Delta_1 + |G_{p1}|^2 / (\Gamma_{10} + i\Delta_1 - i\Delta_{p1} + |G_{p2}|^2 / (\Gamma_{30} + i\Delta_1 - i\Delta_{p1} + i\Delta_{p2} + |G_{p3}|^2 / (\Gamma_{31} + i\Delta_1 - i\Delta_{p1} + i\Delta_{p2} - i\Delta_{p3}))))$

$$d_4 = |G_1|^2 / (\Gamma_{20} + i\Delta'_1 + i\Delta_1 + |G_{p1}|^2 / (\Gamma_{10} + i\Delta'_1 + i\Delta_1 - i\Delta_{p1} + |G_{p2}|^2 / (\Gamma_{13} + i\Delta'_1 + i\Delta_1 - i\Delta_{p1} - i\Delta_{p2} + |G_{p3}|^2 / (\Gamma_{03} + i\Delta'_1 + i\Delta_1 - i\Delta_{p1} - i\Delta_{p2} - i\Delta_{p3}))))$$

By using equations (1-2), we can write the interference terms as

$$|\rho_{S/AS}^{(3)} + \rho_{S/AS}^{(5)} + \rho_{S/AS}^{(7)} + \rho_{S/AS}^{(9)} + \rho_{S/AS}^{(11)}| = (A^2 + B^2 + C^2 + D^2 + E^2 + 2AB\cos(\Delta\varphi_1) + 2AC\cos(\Delta\varphi_2) + 2AD\cos(\Delta\varphi_3) + 2AE\cos(\Delta\varphi_4) + 2BC\cos(\Delta\varphi_5) + 2BD\cos(\Delta\varphi_6) + 2BE\cos(\Delta\varphi_7) + 2CD\cos(\Delta\varphi_8) + 2CE\cos(\Delta\varphi_9) + 2DE\cos(\Delta\varphi_{10}))^{1/2}$$

dressed third-order density matrix can be approximated as the sum of the third-order, fifth-order, and seventh, ninth, and eleventh-order $E_{S/AS}$, governed by dressed SFWM multi-

Fano phase $\Delta\varphi_{S/AS} = \varphi_{S/AS}^{(L)} - \varphi_{S/AS}^{(K)}$ ($L < K$). The total phase $\varphi_{S/AS}^{(j)}$ of generated $E_{S/AS}$ is a sum of the initial phase $\varphi_{S/AS}^{(j)}$, cross-Kerr non-linear phase $\varphi_{S/AS}^{(j)}$, and self-Kerr non-linear phase $\varphi_{S/AS}^{(j)}$ ($\varphi_{S/AS}^{(j)} = \varphi_{S/AS}^{(j)} + \varphi_{S/AS}^{(j)} + \varphi_{S/AS}^{(j)}$). Therefore, multi-Fano interference could be constructive or destructive depending upon the total phase. When the condition is set as $\Delta\varphi_{S/AS} = 0$ ($i = 1$ to 10), which results in 10 bright states. However, at 0 or π ($i = 1$ to 10), the result shows 10 dark states. For the four dark states, the expression can be written as $|\rho_{S/AS}^{(3)} - \rho_{S/AS}^{(5)} - \rho_{S/AS}^{(7)} - \rho_{S/AS}^{(9)} - \rho_{S/AS}^{(11)}|$. The four-Fano is controlled by ten phases ($\Delta\varphi_1 = \pi$, $\Delta\varphi_2 = \pi$, $\Delta\varphi_3 = \pi$, $\Delta\varphi_4 = \pi$, $\Delta\varphi_5 = 0$, $\Delta\varphi_6 = 0$, $\Delta\varphi_7 = 0$, $\Delta\varphi_8 = 0$, $\Delta\varphi_9 = 0$, $\Delta\varphi_{10} = 0$). Equations (1-2) show four-

$$\rho_{S(3)}^{x(3)} = \frac{-iG_1 G_A G_1'}{(\Gamma_{20} + i\Delta_1 + d_5)(\Gamma_{00} + i\Delta_1 - i\Delta_{AS})(\Gamma_{20} + i\Delta_1 + i\Delta_1' - i\Delta_{AS}'))} \frac{1}{(\Gamma_{20} + i\Delta_1 + d_5)(\Gamma_{00} + i\Delta_1 - i\Delta_{AS})(\Gamma_{20} + i\Delta_1 + i\Delta_1' - i\Delta_{AS}'))}} = \rho_{S(3)}^{x(3)} + \rho_{S(3)}^{x(5)} + \rho_{S(3)}^{x(7)} + \rho_{S(3)}^{x(9)}, \quad (7)$$

$$\rho_{AS(3)}^{x(3)} = \frac{-iG_1 G_S G_1'}{(\Gamma_{20} + i\Delta_1 + d_6)(\Gamma_{00} + i\Delta_1 - i\Delta_S)(\Gamma_{20} + i\Delta_1 + i\Delta_1' - i\Delta_S'))} \frac{1}{(\Gamma_{20} + i\Delta_1 + d_6)(\Gamma_{00} + i\Delta_1 - i\Delta_S)(\Gamma_{20} + i\Delta_1 + i\Delta_1' - i\Delta_S'))}} = \rho_{AS(3)}^{x(3)} + \rho_{AS(3)}^{x(5)} + \rho_{AS(3)}^{x(7)} + \rho_{AS(3)}^{x(9)}. \quad (8)$$

Where $d_5 = |G_2|^2 / (\Gamma_{20} + i\Delta_1 + i\Delta_2 + |G_{p1}|^2 / (\Gamma_{10} + i\Delta_1 + i\Delta_2 - i\Delta_{p1} + |G_{p2}|^2 / (\Gamma_{13} + i\Delta_1 + i\Delta_2 - i\Delta_{p1} - i\Delta_{p2})))$. The equations represent three-Fano interference, which originates from the photon1-photon2 continuum state $\rho_{S/AS}^{x(3)}$ and three bound states (photon1 $\rho_{S/AS}^{(5)}$, photon1-phonon1 $\rho_{S/AS}^{(7)}$, photon1-phonon1-phonon2 $\rho_{S/AS}^{(9)}$). Three-Fano has six phases ($\Delta\varphi_1 = \pi$, $\Delta\varphi_2 = \pi$, $\Delta\varphi_3 = \pi$, $\Delta\varphi_4 = 0$, $\Delta\varphi_5 = 0$, $\Delta\varphi_6 = 0$). The interference between continuous and multi-bound states of SFWM multi-Fano appears when the Δ_2 is scanned.

RESULTS AND DISCUSSIONS:

Through the Eu^{3+} : BiPO_4 crystal lattice vibrations, the phonon dressing can control multi-Fano interference. Figure 2a shows the spectral evolution of hybrid signal (FL+SFWM) from single Fano to triple Fano obtained from (0.5:1) Eu^{3+} : BiPO_4 sample by changing GP (5 μs , 500 μs , 1ms) when E_1 is scanned at 300K. The (0.5:1) Eu^{3+} : BiPO_4 crystal exhibits three distinct fine structure energy levels named as $^5D_1 \rightarrow ^7F_1$ (magnetic dipole transition), $^5D_0 \rightarrow ^7F_1$ (magnetic

Fano interference, which originates from an approximate continuous state $\rho_{S/AS}^{(3)}$, photon1 $\rho_{S/AS}^{(5)}$, photon1-phonon1 $\rho_{S/AS}^{(7)}$, photon1-phonon1-phonon2 $\rho_{S/AS}^{(9)}$, photon1-phonon1-phonon2-phonon3 $\rho_{S/AS}^{(11)}$ states. The interference between continuous and multi-bound states of SFWM multi-Fano interference when the Δ_1 is scanned.

B. The non-Hermitian multi-Fano of two lasers

In Λ -type three-level system, third order

$\rho_{S/AS}^{(3)}$ via $\rho_{00}^{(0)} \xrightarrow{E_1} \rho_{20}^{(1)} \xrightarrow{E_{AS}} \rho_{00}^{(2)} \xrightarrow{E_1} \rho_{20(S)}^{(3)}$ and

$\rho_{00}^{(0)} \xrightarrow{E_1} \rho_{20}^{(1)} \xrightarrow{E_S} \rho_{00}^{(2)} \xrightarrow{E_1} \rho_{20(AS)}^{(3)}$, respectively, can be

written as

dipole transition), and $^5D_0 \rightarrow ^7F_3$ (induced electric dipole transition) at the crystal field of about 10^6 volts/cm. The spectral signal recorded at PMT1 (Fig. 2a11) shows three Fano interference resulting from the coexistence of dressing and fine structure energy levels splitting ($^5D_0 \rightarrow ^7F_1$ in Fig. 5g1) whereas three Fano dips (three dark states) come from destructive interference between approximate continuous state ($\rho_{AS(3)}^{(3)}$)

and three bound states ($\rho_{AS(3)}^{(5)}$, $\rho_{AS(3)}^{(7)}$, $\rho_{AS(3)}^{(9)}$) and

is controlled by Fano phase ($\Delta\varphi_1 = \pi$, $\Delta\varphi_2 = \pi$, $\Delta\varphi_3 = \pi$) modeled through Eqs. (3-4). It is

noteworthy that the magnitudes of the two Fano peaks are greater than those of the three Fano dips because of more pronounced splitting of energy levels within the 7F_1 state compared to the nested three dressing.

$|G_1|^2 / (\Gamma_{20} + i\Delta_1 + |G_{p1}|^2 / (\Gamma_{10} + i\Delta_1 - i\Delta_{p1} + |G_{p2}|^2 / (\Gamma_{13} + i\Delta_1 - i\Delta_{p1} - i\Delta_{p2})))$ from Eqs. (3-4). The validation of this is supported by our

theoretical findings as illustrated in Figure 2h3 at $\Delta_1 = -50$. When the gate position approaches 1ms,

the three suppression Fano dips (Fig. 2a31) become more prominent compared to the enhancement Fano peaks. This observation can be attributed to the dominance of nested three dressing in the completion between energy levels splitting and dressing. In Fig. 2a21, the first Fano dip is stronger than the third Fano dip which can be attributed to the greater influence of the linear polarization dipole moment in energy level ${}^7F_{1, MJ=0}$ in comparison to the circular partial dipole moment in energy level ($\mu_L > \mu_C$). Our theoretical results (Figs. 2g and 2h) validate the multi-Fano evolution (Fig. 2a). In Fig. 2a12, two Fano interference results from the coexistence of double dressing and energy levels splitting (${}^5D_0 \rightarrow {}^7F_1$), where two Fano dips come from interference in an approximate continuous state $\rho_{S(2)}^{(3)}$ and two bound states $\rho_{S(2)}^{(5)}, \rho_{S(2)}^{(7)}$ controlled by Fano phase ($\Delta\phi_1 = \pi, \Delta\phi_2 = \pi$). The practical results obtained align precisely with the theoretical results depicted in Fig. 2h2. (Simulated at $\Delta_1 = -50$). When the GP increases to 500 μ s (Fig. 2a22), the two Fano dips evolve into three Fano dips due to sensitive phonon dressing ($|G_{p1}|^2, |G_{p2}|^2$) and easy distinction for in-phase SFWM. When GP is at 1ms (Fig. 2a23), the right first Fano dip is strongest due to more dressing interaction of ${}^7F_{1, MJ=0}$ and ${}^7F_{1, MJ=+1}$. The single

Fano interference (Fig. 2a13), occurs due to the coexistence of single dressing and energy level splitting. In contrast, a single Fano dip emerges from the interference between dark states and bright states, a phenomenon regulated by the Fano phase ($\Delta\phi = \pi$) and modeled by $\rho_{AS(1)}^{(3)} + \rho_{AS(1)}^{(5)}$.

When GP is at, single Fano dip increases in comparison to two Fano peaks due to photon dressing ($|G_1|^2$) dominance.

The spectral evolution of two sharp peaks to five Fano interference, recorded at PMT2 by adjusting GP, is displayed in Fig. 2b. The two sharp peaks observed in Figs. 2b11, 2b12, and 2b13 can be attributed to the splitting of energy levels during the transitions $5D1 \rightarrow 7F1$, $5D0 \rightarrow 7F1$, and $5D1 \rightarrow 7F3$, respectively. Multi-Fano interference seen at PMT2 (Fig. 2b) is stronger than at PMT1 (Fig. 2a) because of the strong SFWM at the near detector. The Spectral evolution observed at PMT3 (Fig. 2c) exhibits behavior that is identical to that shows similar behavior as observed at PMT1. The Fano interference in Figs. 2d-2f, resulting from the interaction of two lasers, is stronger compared to that of a single laser (Figs. 2a-2c), mostly due to two lasers dressing enhancement. However, the left first Fano dip is stronger than the left third Fano dip in Fig. 2d, f due to more dressing interaction effect between ${}^7F_{1, MJ=+1}$ and ${}^7F_{1, MJ=0}$.

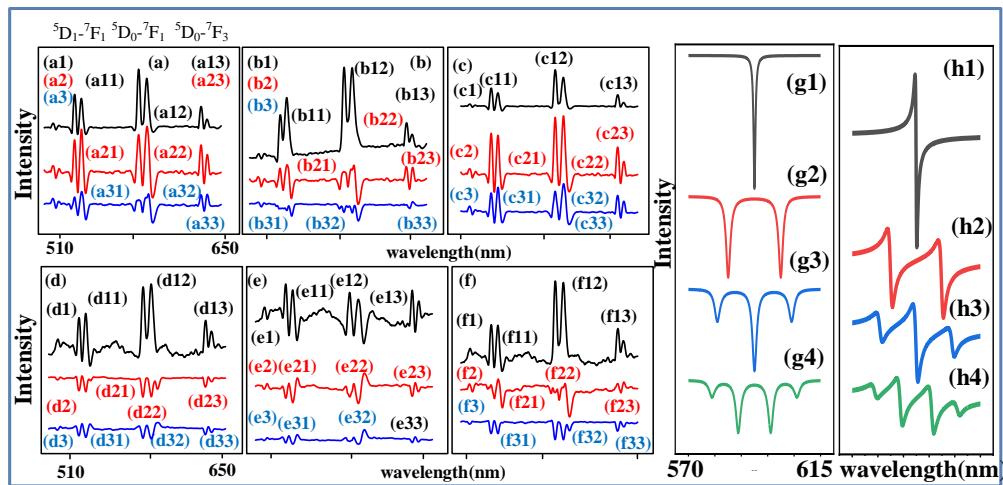


Fig. 2 Spectral intensity signal measured from Eu^{3+} : BiPO_4 crystal with molar ratio (0.5:1) by scanning E_1 ; **a** PMT1; **b** PMT2 and **c** PMT3. **a1-a3** the spectral signal intensity measured at different gate positions (5 μs , 500 μs , and 1ms). **b1-b3**, **c1-c3** are the same GP as **a1-a3**. **d**, **e** and **f** Spectral intensity from (0.5:1) Eu^{3+} : BiPO_4 measured at PMT1, PMT2, and PMT3, respectively, when E_1 is scanned while E_2 is fixed at 588nm (Laser power=7mW, temperature=300k, gate width = 200ns). **g** and **h** Theoretical results for dressing evolution corresponding to **2a** at $\Delta_1=0$ and corresponding **3a** at $\Delta_1=-50$, respectively.

Figure 3a shows the spectral evolution of multi-Fano interference from three Fano dips to a single Fano dip in (7:1) Eu^{3+} : BiPO_4 crystal when E_1 is scanned. In Fig. 3a11, two Fano peaks and three Fano dips come from nested three dressing

$$\left(|G_1|^2 / \Gamma_{20} + i\Delta_1 + |G_{p1}|^2 / (\Gamma_{10} + i\Delta_1 - i\Delta_{p1} + |G_{p2}|^2 / (\Gamma_{30} + i\Delta_1 - i\Delta_{p1} + i\Delta_{p2})) \right)$$

controlled through the Fano phase ($\Delta\varphi_1=\pi$, $\Delta\varphi_2=\pi$, $\Delta\varphi_3=\pi$), corresponding to the simulation

in Fig. 2g3. The Hamiltonian ($H = i\hbar\kappa_1\alpha_1^\dagger\alpha_{p1}^\dagger\alpha_{p2}^\dagger$

where $\kappa_1 = -i\varpi\chi_1^{(9)}E_3E_{p1}E_{p2}E_1^3/2$) shows strong dressing coupling between photon1 (α_1^\dagger), sample phonon1 (α_{p1}^\dagger), and sample phonon2

(α_{p2}^\dagger). The energy level splitting ($^5\text{D}_0$ - $^7\text{F}_3$) and

dressing coexistence lead to two Fano interferences in Fig. 3a12, where two Fano dips can be explained by nested two dressing

($|G_1|^2 / \Gamma_{20} + i\Delta_1 + |G_{p1}|^2 / (\Gamma_{10} + i\Delta_1 - i\Delta_{p1})$) controlled by

Fano phase ($\Delta\varphi_1=\pi$, $\Delta\varphi_2=\pi$) mentioned in Eqs. (1-2). The amplitude of three Fano dips (Fig. 3a11) reduces as a consequence of the weak dressing resulting from the interaction of two lasers, when compared to Fano dips illustrated in Figure 3a11. Similarly, the two Fano interference becomes weak in Fig. 3a22 which aligns with the simulation results depicted in Fig. 2g2. When compared to the Fano interference in Fig. 3a11, the Fano interference seen in Fig. 3a3 is weak. This difference can be attributed to the influence of a narrower excitation band, which controls the extent of crystal vibration phonons in the system.

In Fig. 3b1, two sharp peaks result from competition between energy level splitting ($^5\text{D}_0$ -

$^7\text{F}_1$) dominance and dressing which can be further explained by two lasers interaction and low-intensity phonon dressing ($|G_{p1}|^2$, $|G_{p2}|^2$) at

low temperatures. Moreover, the spectral linewidth of the peak is sharp (Fig. 3b1). The four Fano dips (Fig. 3b2) come from destructive interference ($\rho_{S/AS}^{(3)} + \rho_{S/AS}^{(5)} + \rho_{S/AS}^{(7)} + \rho_{S/AS}^{(9)} + \rho_{S/AS}^{(11)}$ from Eqs. (5-6)). The control of Fano dips and peaks can be achieved by manipulating the Fano phase where the dips are attributed to the presence of four dark states that are observed at $\Delta\varphi_1=\Delta\varphi_2=\Delta\varphi_3=\Delta\varphi_4=\pi$. Such four dressing dips come from photon1 dressing $|G_1|^2$ and three phonons dressing ($|G_{p1}|^2$, $|G_{p2}|^2$, $|G_{p3}|^2$) with

Hamiltonian $H = i\hbar\kappa_1\alpha_1^\dagger\alpha_{p1}^\dagger\alpha_{p2}^\dagger\alpha_{p3}^\dagger + H.c.$ where

$\kappa_1 = -i\varpi\chi_1^{(11)}E_{AS}E_SE_{p1}E_1^3E_{p2}E_{p3}/2$. It shows the strong

dressing coupling among photon1 (G_1^\dagger)-phonon1 (G_{p1}^\dagger)-phonon2 (G_{p2}^\dagger)-phonon3 (G_{p3}^\dagger). In Fig. 3b2,

broad profile linewidth is caused by three phonons dressing in (0.5:1) BiPO_4 . The Fano phase for four dark states and six bright states can be written as $\Delta\varphi_1=\Delta\varphi_2=\Delta\varphi_3=\Delta\varphi_4=\pi$ and $\Delta\varphi_5=\Delta\varphi_6=\Delta\varphi_7=\Delta\varphi_8=\Delta\varphi_9=\Delta\varphi_{10}=0$, respectively. The presence of six bright states surpasses the number of four dark states due to the additional bright state being integrated into the existing five bright states. The left first Fano dip is stronger than the left fourth Fano dip in Fig. 3b2 due to $\mu_c > \mu_L$. These results correspond to our theoretical results obtained for nested four dressing at $\Delta_1=50$.

In Fig. 3b3, the signal observed by scanning E_1 while fixing E_2 (588nm) shows multi-Fano

interference with three Fano dips resulting from nested three dressings

$$\left(|G_2|^2 / (\Gamma_{20} + i\Delta_2 + |G_{p1}|^2 / (\Gamma_{10} + i\Delta_2 - i\Delta_{p1})) + |G_{p2}|^2 / (\Gamma_{30} + i\Delta_2 - i\Delta_{p1} + i\Delta_{p2})) \right) \text{ in Eqs. (7-8)}$$

and four Fano peaks from energy level splitting and Autler–Townes (AT) splitting. In addition, it is observed that single laser excitation (Fig. 3b2) exhibits a greater number of dressing dips compared to two lasers excitation (Fig. 3b3). This can be attributed to the interaction between the two lasers within the crystal, which reduces the dressing effect, as illustrated in Fig. 2e. The observed outcome is consistent with the findings obtained from the nested three-dressing simulation. at $\Delta_1 = 50$. The spectral signal depicted in Fig. 3b4 exhibits strong three Fano interference at $15\mu\text{s}$ gate width for (0.5:1) Eu^{3+} : BiPO_4 sample mostly attributed to the dominance of SFWM dominance. The three multi-Fano dips can be explained by photon2 and two phonons nested dressing ($|G_2|^2$, $|G_{p1}|^2$, $|G_{p2}|^2$). By comparing the Fano dips observed in

Fig. 3b3 to those in Fig. 3b4, it is evident that the latter exhibit three consecutive Fano dips. This can be attributed to an more phonon dressing. As gate width increases from $200\mu\text{s}$ (Fig. 3b3) to 500ns (Fig. 3b4), the increasing ratio of SFWM in hybrid signal causes high spectral resolution. The bright and dark states can be controlled by adjusting the phase between zero and π . As the gate width expands, the number of bright states rises, as illustrated in Fig. 3b4. The three Fano dips and four Fano peaks originate from two laser excitation with a Fano phase of three dark states ($\Delta\varphi_1=\Delta\varphi_2=\Delta\varphi_3=\pi$) and three bright states ($\Delta\varphi_4=\Delta\varphi_5=\Delta\varphi_6=0$), respectively. The additional peak comes from pure constructive states at Fano phases $\Delta\varphi_i=0$ ($i=1,2,3,4,5,6$). When the GP reaches to 1ms , Fig. 3b5 depicts clearly defined sharp peaks that can be attributed to the dominance of crystal field splitting, as illustrated in Fig. 1a2. Based on the findings obtained from our research, it can be concluded that the (0.5:1) H-phase Eu^{3+} : BiPO_4 exhibits strong dressing Fano interference as compared to (7:1) M-phase Eu^{3+} : BiPO_4 due to more phonon dressing.

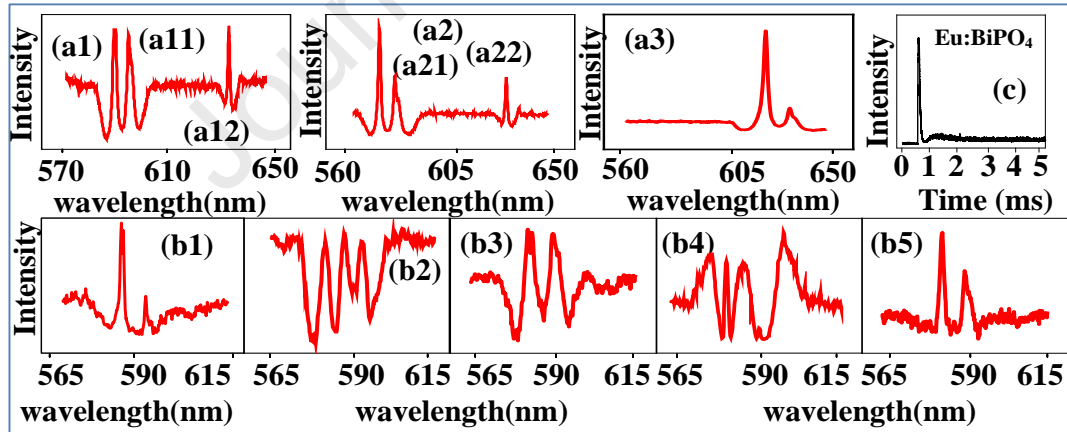


Fig. 3 a Measured spectral intensity of the hybrid signal from (7:1) phase Eu^{3+} : BiPO_4 at PMT1 by fixing GP ($30\mu\text{s}$), gate width (500ns), and temperature (300K). **a1** Scan E_2 only, **a2** Scan E_1 while E_2 is fixed at 588nm ; **a3** Scan E_2 only. **b** Measured Spectral from (0.5:1) Eu^{3+} : BiPO_4 at PMT2 and 9mW power. **b** GP ($500\mu\text{s}$), and gate width (200ns). **b1** Scanning E_1 while fixing E_2 (588nm) and low temperature (77K); **b2** Scanning E_1 only at 300K ; **b3** Scan E_1 is scanned while E_2 is fixed at 588nm at room temperature (300K). **b4** Scan E_1 is scanned and E_2 (588nm), GP ($500\mu\text{s}$), gate width ($15\mu\text{s}$) and 300K temperature; **b5** Scanning E_1 at GP (1ms), gate width (200ns) and 300K temperature.

Figures 4a and 4b discuss the evolution of SFWM from FL in a hybrid signal for (6:1) and (1:1) $\text{Eu}^{3+}:\text{BiPO}_4$, respectively. At near GP, the dressing effect is weak, leading to a spectral peak characterized by low resolution and a broad linewidth, as shown in Fig. 4a1. Upon increasing the GP (20 μs), an emergence of three Fano dips and two Fano peaks is apparent, (Fig. 4a2), resembling the pattern depicted in Fig. 2a22. The observed phenomenon can be attributed to the reduced impact of dressing detuning, resulting in a decreased photon dressing effect and high SFWM resolution. By further increasing GP (200 μs), the three Fano dips become stronger in Fig. 4a3 due to one photon dressing ($|G_1|^2$) and two phonon dressings ($|G_{p1}|^2, |G_{p2}|^2$) as modeled from Eqs (3-4). As the GP reaches 500 μs , the five Fano-dips in Fig. 4a4 originate from energy levels $^7\text{F}_1$ symmetrical splitting of one laser excitation.

Figure 4b shows the evolution from a single broad dip to sharp multi-dips for (1:1) $\text{Eu}^{3+}:\text{BiPO}_4$ under the same experimental conditions as described in Fig. 4a. In comparison to Fig. 4a1, the broad dip is shown in Fig. 4(b1) due to higher frequency (w_{pi}) phonon for (1:1) than (6:1) $\text{Eu}^{3+}:\text{BiPO}_4$, which results in strong phase transition phonon dressing ($|G_{pi}|^2 / (i\Omega_{mm} - iw_{pi})$) with $\Delta_1 - \Delta_{p1}$, $\Delta_1 - \Delta_{p1} + \Delta_{p2}$, $\Delta_1 - \Delta_{p1} + \Delta_{p2} - \Delta_{p3}$, which is close to resonance compared with (6:1) sample in Fig. 4a. As GP reaches 500 μs , the five Fano dips are shown in Fig. 4b4. So, the phase transition phonon dressing is stronger in the (1:1) sample than in the (6:1) sample. In summary, in contrast

to the FL signal, the SFWM signal exhibits higher resolution. The presence of multiple Fano dips can be readily observed in the signal generated by SFWM).

From our results, we have realized the wavelength division multiplexing of both classical and coherent channels. The non-classical SFWM may be effectively multiplexed with divided Fano dip across a range of 1 μs to 500 μs . This multiplexing technique enables the routing of identical information across many channels, ranging from one channel (Fig. 4b1) to five channels (Fig. 4b4). A non-Hermitian multi-channel router can be realized by non-Hermitian control real part quantization (Fig. 1c), and the routing process can be achieved by changing the boxcar gate position. Similarly, when GP is at 500 μs , the coherent channel output can be multiplexed to five divided Fano dips for routing the same information to different channels. Fig. 4b shows two adjacent dips with relative distance between many dips. Such a phenomenon (pure dip to five Fano dip) is analogous to routing. Such results are used for routing. Here we use, channel equalization ratio

$$(P = 1 - \sqrt{\sum_{i=1}^{N-1} (s_i - a)^2 / a}) \text{ to measure de-}$$

multiplexing, where a is the area of one dip and s_i is the area of each dip or gap between dips. When $s_i \approx a$ P is maximum (100%) and we get more balanced and stable spatial channels. From Fig. 4b, the channel equalization ratio P has the potential to reach values ranging from 60% to 80%.

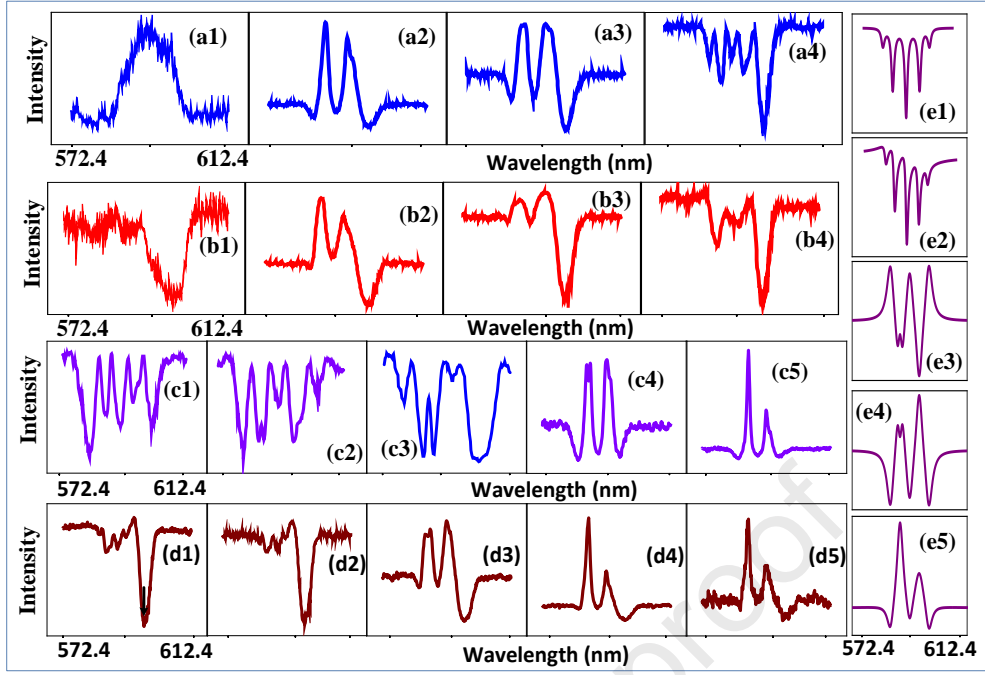


Fig. 4 **a** and **b** Spectral intensity of hybrid signal measured at PMT1 from (6:1) and (1:1) Eu^{3+} : BiPO_4 crystal, respectively, by scanning Δ_1 with gate position being $1\mu\text{s}$, $20\mu\text{s}$, $200\mu\text{s}$, and $500\mu\text{s}$. **c** and **d** Spectral intensity of (0.5:1) and (1:1) Eu^{3+} : BiPO_4 crystal versus Δ_1 by increasing power of E_1 from 9mW to 1mW, respectively. **e** Theoretical results corresponding to **c**.

Next, Figs. 4c and 4d represent the spectrum evolution from multi-Fano interference to two sharp peaks for (0.5:1, 1:1) BiPO_4 respectively, versus changing power. In Fig. 4c, the spectral intensity for the (0.5:1) Eu^{3+} : BiPO_4 sample is shown at the near detector (PMT2). The laser power was changed from 9mW to 1mW at 300K. When the power is high, strong $|G_1|^2$ results in five dressing dips (Figs. 4c1, 4c2) from 7F_1 symmetrical splitting (similar to Fig. 4a4), correspond to the simulation result at $\Delta_1=0$ in Figs. 4e1-4e2, respectively. Also, the left first to third Fano dip for energy level ${}^7F_{1, MJ=\pm 1}$ in Figs. 4c1-4c2 come from nested three dressings, where the left fourth to fifth Fano dips come for energy level ${}^7F_{1, MJ=\pm 1}$ in Figs. 4c1-4c2 owing to nested double dressing. Fig. 4d shows the spectral intensity for (1:1) Eu^{3+} : BiPO_4 at PMT2 by changing power (9mW, 7mW, 5mW, 3mW, 1mW). When the power of E_1 decreases to 1mW, the two sharp peaks are shown in Fig. 4c5 and 4d5 due to weak dressing ($|G_1|^2 \approx 0$) at low power.

The nested dressing multi-Fano dips observed in our studies can be associated with third-order quantization, as depicted in Figure 1d [20-22]. Herein, we discuss exceptional points (EP) or non-Hermitian control originating from real and imaginary quantization alignment as shown in Fig. 1d. The non-Hermitian exceptional point (EP) manifests itself via crystal field splitting independently of any dressing effects. Figures 4a,b and 4c,d exhibits full- and half-EP control, respectively. The multi-Fano real part quantization channels can be defined as $N = N_m / N_{EP}$, where N_m represents the number of dressing dips in SFWM signal, N_{EP} is the number of peaks at EP control (two CF peaks), where each peak represents one level (${}^7F_{1, MJ=\pm 1}$, or ${}^7F_{1, MJ=0}$). The SFWM multi-Fano quantization exhibits owing channel $N=3$ (fourth-order) at ${}^7F_{1, MJ=\pm 1}$ for the left EP peak (Fig. 4a4 to Fig. 4a2 and $N=2$ (third-order) at ${}^7F_{1, MJ=0}$ for the right EP peak (Fig. 4c5 to Fig. 4c1). Similarly, $N=1$ (second-order) at ${}^7F_{1, MJ=0}$, and third-order $N=2$ at

${}^7F_{1, MJ=\pm 1}$ exhibited from each level in Fig. 4b and $N=2$ (third-order) exhibited in each level from Fig. 4d.

Figure 5 shows the evolution from multiple dips to two peaks when the laser of E_1 is kept high. Figures 5a and b show five Fano dips resulting from five nested dressings (three dressing in ${}^7F_{1, MJ=\pm 1}$ and two dressing in ${}^7F_{1, MJ=0}$) in a similar manner to that described in Fig. 4c1. When the laser power is lowered, there is a reduction in photon dressing, which leads to the diminishing of three Fano dips resulting from three distinct fine structure energy levels (${}^7F_{1, MJ=-1}$, ${}^7F_{1, MJ=0}$, ${}^7F_{1, MJ=1}$). This reduction in photon dressing causes the phenomenon illustrated in Fig. 4c4 to also decrease. When the power reaches 1mW, only two sharp peaks appear in Fig. 5a4, b4, c4 due to weak photon dressing. From Figs. 5a1 to 5a4, the

center of the peak remains unchanged due to strong phonon dressing. When comparing the signal measurements of PMT2 with PMT1 and PMT3, it is observed that the signal measured at PMT2 exhibits a stronger dressing effect. This can be attributed to its proximity to the sample, allowing it to detect fluorescence with a higher amplitude, resulting in a more significant dressing dip. Theoretical results are displayed in Figure 5d in accordance with experimental results (Fig. 5b).

Owing to the above explanations, figure 5 shows similar EP control for SFWM multi-Fano quantization (half-EP control). Figure 5b1 shows channel $N=3$ (fourth-order) at ${}^7F_{1, MJ=\pm 1}$ for the left EP peak 5b4 and exhibit $N=2$ (third-order) at ${}^7F_{1, MJ=0}$ in 5b1 for the right EP peak (5b4). Similar results were observed for Figs. 5a, c.

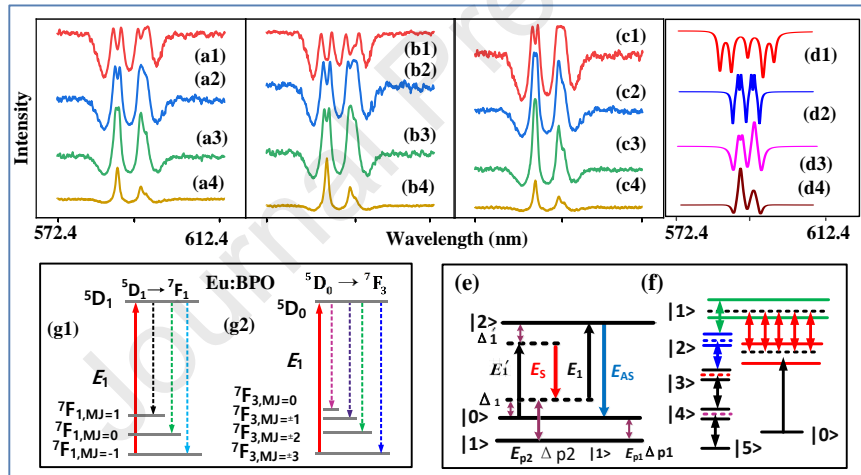


Fig. 5 a-c Spectral intensity of the hybrid signal from (0.5:1) $\text{Eu}^{3+}:\text{BiPO}_4$ plotted versus Δ_1 by increasing E_1 power measured at PMT1, PMT2, and PMT3, respectively, at fixed gate width (200ns), gate position (500μs) and temperature (300K). d Theoretical results by scanning Δ_2 from -50 to 50 and fixing Δ_1 at -500, -250, 0, 250 to 500. e SFWM dressing energy level. f Five nested dressing energy levels. g1-g2 Fine structure energy level diagram of $\text{Eu}^{3+}:\text{BiPO}_4$ for transition ${}^7F_1 \rightarrow {}^5D_1$ and ${}^7F_3 \rightarrow {}^5D_0$, respectively.

Figure 6a shows the EP evolution vs the ratio (G_{p1}/Γ_{20}) between photon-phonon dressing Rabi-frequency and transverse de-phase rate between level $|2\rangle$ and $|0\rangle$. The theoretical results correspond to nested double dressing. At $G_{p1}/\Gamma_{20}=0.5$, one energy level splits into a real part and an imaginary part, respectively. At internal dressing $G_1/\Gamma_{20}=0.5$, the real and imaginary parts are split in Figs. 6a3, a4, respectively. The splitting of the real part and the

imaginary part of the nested double dressing does not occur simultaneously. When the third-order splitting (G_1/Γ_{20}) occurs in the real part (Fig. 6a3), the corresponding imaginary part (Fig. 6a4) will have the second-order splitting (G_{p1}/Γ_{20}). Thus, the real part splitting is larger than the imaginary part splitting. The imaginary part is nonlocal, more degenerate and non-Abelian, and highly symmetric. The real part is local, less degenerate and Abelian, and low symmetric.

More importantly, the real part is changed from local, Abelian, and more degenerate to non-local, non-Abelian, and less degenerate in third-order systems. The dominance of real part splitting ($G > \Gamma$) shows high-order router, however, the dominance of imaginary part splitting ($\Gamma > G$) shows low-order router. The non-Hermitian Exception Point (EP) is a point without dressing. Such exceptional point can be achieved by varying various external parameters. Such EP can be achieved by changing different external parameters. The GP is the primary parameter. When the GP is changed from middle (hybrid) to far (SFWM), there is an existence of the EP between hybrid and SFWM. For the nested double dressing, the dressing term is already solved, and it is converted into a univariate cubic equation to be solved, so three eigenvalues are obtained. But in our model, the photon dressing like Zeeman splits three energy levels in Fig. 1a4. The ${}^7F_{1, MJ=-1}$ and ${}^7F_{1, MJ=+1}$ energy levels are nested dressed by two phonons (phonon1 and phonon2) and the other two phonons (phonon3 and phonon4), respectively. One photon (photon1) dressed ${}^7F_{1, MJ=0}$ energy level. So, eight eigenvalues can be obtained by solving the equations of two nested double dressing and one single dressing. Moreover, our experimental results are a subset of the theoretical simulation.

Figures 6c, d show the spectral intensity signal obtained from (0.5:1) Eu^{3+} : BiPO_4 (C_2 symmetry) and H-phase Eu^{3+} : NaYF_4 (C_s symmetry), respectively. In this experiment, the competition between real a and imaginary ib eigenvalues based on nested photon-phonon dressing is discussed. The detailed model of EPs control based on different laser dressing are depicted in Table S1 to S4 (supplementary file). It is worth mentioning that the GP affects the de-phase rate (Γ) at the spectral signal. In other words, the ratio of G and Γ can be tuned by changing the GP. In Figs. 4c, Fig. 5b1, and Fig. 6c1, one can observe the visible five Fano dips due to the dominance of the nested dressing ($|G_1|^2, |G_{p1}|^2$,

$|G_{p2}|^2, |G_{p3}|^2$ in Eqs. (5-6)). The left first and second Fano dips come from phonon1 and phonon2 dressing. The central Fano dip results from photon1 dressing. The fourth and fifth Fano dips can be explained by phonon3 and phonon4 dressing. Compared to the other four Fano dips, the fifth Fano dip is the strongest (Figs. 4a4) due to photon dressing (similar to Figs. 4c1, c2 and 5a1, b1).

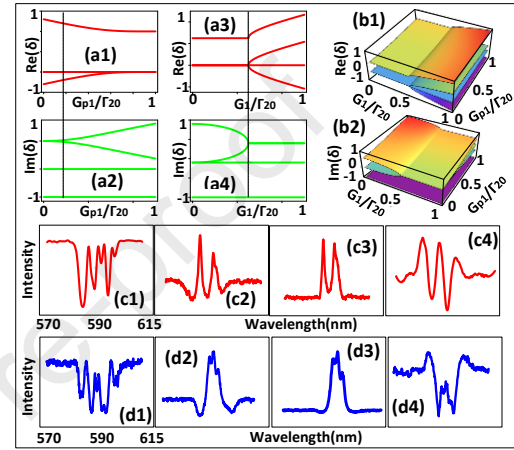


Fig. 6 **a1, a3** Real and **a2, a4** imaginary parts of the eigenvalues as a function of the dressing Rabi-frequency (G) and transverse de-phase rate (Γ) with a Gaussian-like envelope. **b1, b2** show 3D simulation corresponding to 2D simulation **a1-a2, a3-a4**, respectively. The spectral signal measured at PMT2 obtained from **c, d**; (0.5:1) sample of Eu^{3+} : BiPO_4 and Eu^{3+} : NaYF_4 when E_1 is scanned from 572.4 nm to 612.4nm and GP is changed (**c** (500 μ s, 2ms, 5ms, 20ms) and **d** (1ms, 6ms, 10ms, 25ms)) at 200ns gate width and 300 K temperature at power= 9mW, respectively.

When the GP reaches 5ms, one can observe the two sharp peaks in Fig. 6c3 corresponding to EP where G and Γ are equal due to the dominance of crystal field splitting (Fig. 1a2), validated by theoretical results in Fig. 6(a). The visible three Fano dips observed in Fig. 2a12, Figs. 4a2, b2 and Fig. 6c3 are attributed to the stronger nested three dressing (photon1-phonon1-phonon2 atomic coherence coupling in Fig. 1a4) than crystal field splitting. The evolution from three Fano dips to two sharp EP peaks, to five Fano dips corresponds to Figs. 1a2, a4. Figures 6b1 and b2 are the 3D simulation results

corresponding to the real and imaginary parts of 2D simulations (Fig. 6a and b), respectively.

Lastly, Fig. 6c exhibits fourth-order ($N=3$) at ${}^7F_{1, MJ=\pm 1}$, which corresponds to four eigenvalues in a univariate quartic equation (S4 Galois group) [38] with three dressing, and one third-order ($N=2$) EP control at ${}^7F_{1, MJ=\pm 1}$ corresponding to four eigenvalues in a univariate cubic equation (S3 Galois group) with two dressing for left and right peak, respectively. Figure 6d1-d4 exhibits one third-order ($N=2$) EP control for each peak.

CONCLUSION

In summary, this research examined the phenomenon of multi-Fano dips and demonstrated that their behavior can be regulated by higher-order exceptional points control in non-Hermitian systems. Additionally, we demonstrated the relationship between multi-Fano interference and the photon-phonon nested dressing effect for various Eu^{3+} : BiPO_4 samples. This research establishes the categorization of the multi-Fano resonance between discrete and continuous states into three distinct types (dressed MFL, hybrid, and dressed SFWM Fano interference), which can be controlled through the gate position (ratio of MFL and Stokes). Moreover, our experimental results suggest a scheme to achieve a higher channel equalization ratio of about 80%.

Funding. This work was supported by the National Key Research and Development Program of China (2017YFA0303700, 2018YFA0307500), Key Scientific and Technological Innovation Team of Shaanxi Province (2021TD-56), National Natural Science Foundation of China (61975159, 11904279, 12174302, 62022066, 12074306, 12074303).

Data Availability. All data generated or analyzed during this study are included in this published article.

Declarations. The authors declare that they have no conflict of interest.

REFERENCES

1. U. Fano. Effects of Configuration Interaction on

- Intensities and Phase Shifts. *Phys. Rev.* **124**, 1866-1878 (1961). <https://doi.org/10.1103/PhysRev.124.1866>.
2. F. L. Mikhail, V. R. Mikhail, N. P. Alexander and S. K. Yuri. Fano resonances in photonics. *Nat. Photon.* **11**, 543–554 (2017). <https://doi.org/10.1038/nphoton.2017.142>.
3. L. Philippe, Y. Wei, V. Kevin, S. Christophe and H. Jean-Paul. Light Interaction with Photonic and Plasmonic Resonances. *Laser. Photon. Rev.* **12**. 1700113 (2018). <https://doi.org/10.1002/lpor.201700113>.
4. W. X. Lim, M. Manjappa, P. Pitchappa and R. Singh. Shaping High-Q Planar Fano Resonant Metamaterials toward Futuristic Technologies. *Adv. Optical. Mater.* **6**, 1800502 (2018). <https://doi.org/10.1002/adom.201800502>.
5. M. Kroner, A. O. Govorov, S. Remi, B. Biedermann, S. Seidl, A. Badolato, P. M. Petroff, W. Zhang, R. Barbour, B. D. Gerardot, R. J. Warburton and K. Karrai. The nonlinear Fano effect. *Nature.* **451**, 311-314 (2008). <https://doi.org/10.1038/nature06506>.
6. C. Ott, A. Kaldun, P. Raith, K. Meyer, M. Laux, J. Evers, C. H. Keitel, C. H. Greene and T. Pfeifer. Lorentz Meets Fano in Spectral Line Shapes: A Universal Phase and Its Laser Control. *Science.* **340**, 716-720 (2013). <https://doi.org/10.1126/science.1234407>.
7. M. I. Stockman. Dark-hot resonances. *Nature.* **467**, 541–542 (2010). <https://doi.org/10.1038/467541a>.
8. M.F. Limonov. Fano resonance for applications. *Adv. Opt. Photon.* **13**, 703–771 (2021). <https://doi.org/10.1364/AOP.420731>.
9. H. Beutler and A. V. A. Über Absorptionsserien. Krypton und Xenon zu Termen zwischen den beiden Ionisierungsgrenzen $2P_{03/2}$ und $2P_{01/2}$. *Z. für Phys.* **93**, 177–196 (1935). <https://doi.org/10.1007/BF01365116>.
10. S. L. Sorensen, T. Åberg, J. Tulkki, E. Rachlew-Källne, G. Sundström, and M. Kirm. Argon 3s autoionization resonances. *Phys. Rev. A.* **50**, 1218 (1994). <https://doi.org/10.1103/PhysRevA.50.1218>.
11. H. Hossein, U. H. Absar, S. Wittek, H. Garcia-Gracia, Ramy El-Ganainy, D.N. Christodoulides. Enhanced sensitivity at higher-order exceptional points. *Nature.* **548** (7666), 187–191 (2017). <https://doi.org/10.1038/nature23280>.
12. Y. S. Wang, Y. H. Ren, X. X. Luo, B. Li, Z. Y. Chen, Z. Z. Liu, F. Liu, Y. Cai, Y. P. Zhang, J. Liu, and F. Li. Manipulating cavity photon dynamics by topologically curved space. *Light. Sci. Appl.* **11**, 308 (2022). <https://doi.org/10.1038/s41377-022-01009-x>.
13. B.Q. Ren, A. A. Arkhipova, Y. Q. Zhang, Y. V. Kartashov, H. G. Wang, S. A. Zhuravitskii, N. N. Skryabin, I. V. Dyakonov, A. A. Kalinkin, S. P. Kulik, V. O. Kompanets, S. V. Chekalin, and V. N. Zadkov. Observation of nonlinear disclination states. *Light. Sci. Appl.* **12**, 194 (2023). <https://doi.org/10.1038/s41377-023-01235-x>.
14. M. A. Miri and A. Alu. Exceptional points in optics and photonics. *Science.* **363**, 6422 (2019). <https://doi.org/10.1126/science.aar7709>.
15. H. D. Wu, Y.P. Ruan, Z. X. Li, M. X. Dong, M. Cai, J. S. Tang, L. Tang, H. Zhang, M. Xiao, and K. Y. Xia. Fundamental distinction of electromagnetically induced transparency

- and Autler-Townes splitting in breaking the time-reversal symmetry. *Laser & Photonics Reviews*. **16**, 2100708(2022).<https://doi.org/10.1002/lpor.202100708>.
16. B. Midya, H. Zhao and F. Liang. Non-Hermitian photonics promises exceptional topology of light. *Nat. Commun.* **9**, 2674(2018). <https://doi.org/10.1038/s41467-018-05175-8>.
 17. D. L. Zhu, S. Liu, R.Q. Fan, S.M. Xiao and Q.H. Song. Unidirectional emission from a PT-symmetric annular microcavity. *Phy. Rev. A*, **99**(3), 033849(2019). <https://doi.org/10.1103/PhysRevA.99.033849>.
 18. Z. Y. Zhang, Y. Liu, J. L. Feng, J. T. Sheng, Y. Q. Zhang, Y. P. Zhang and M. Xiao. Parity-Time-Symmetric Optical Lattice with Alternating Gain and Loss Atomic Configurations. *Laser & Photonics Reviews*. **12**(10), 1800155(2018).<https://doi.org/10.1002/lpor.201800155>.
 19. A. Krasnok, M. Tymchenko, A. Alù. Nonlinear metasurfaces: a paradigm shift in nonlinear optics. *Mater. Today*. **21**, 8(2018). <https://doi.org/10.1016/j.mattod.2017.06.007>.
 20. K. Koshelev, S. Kruk, E. Melik-Gaykazyan, J-H. Choi, A. Bogdanov, H-G. Park and Y. Kivshar. Subwavelength dielectric resonators for nonlinear nanophotonics. *Science*. **367**, 288–292 (2020). <https://doi.org/10.1126/science.aaz3985>.
 21. G. Z. Liang, X. C. Yu, X. N. Hu, B. Qiang, C.W. Wang and Q.J. Wang. Mid-infrared photonics and optoelectronics in 2D materials. *Mater. Today*. **51**, 294–316(2021). <https://doi.org/10.1016/j.mattod.2021.09.021>.
 22. A. H. Safavi-Naeini, T. P. M. Alegre, J. Chan, M. Eichenfield, M. Winger, Q. Lin, J. T. Hill, D. E. Chang and O. Painter. Electromagnetically induced transparency and slow light with optomechanics. *Nature*. **472**, 69–73(2011). <https://doi.org/10.1038/nature09933>.
 23. Y. Kim, J. Lee. Ultrafast dynamics of phase and topology in Dirac semiconductors. *Mater. Today Phys.* **21**, 100525 (2021).<https://doi.org/10.1016/j.mtphys.2021.100525>.
 24. B. Zhen, S. L. Chua, J. Lee, A. W. Rodriguez, X. D. Liang, S. G. Johnson, J. D. Joannopoulos, M. Soljacic and O. Shapira. Enabling enhanced emission and low-threshold lasing of organic molecules using special Fano resonances of macroscopic photonic crystals. *Proc. Natl. Acad. Sci. USA*. **110**(34), 13711–13716 (2013). <https://doi.org/10.1073/pnas.1311866110>.
 25. Y. Yu, W. Q. Xue, E. Semenova, K. Yvind and J. Mork. Demonstration of a self-pulsing photonic crystal Fano laser. *Nat. Photon.* **11**, 81–84(2017).<https://doi.org/10.1038/nphoton.2016.248>.
 26. C. C. Lu, H. Y. Yuan, H. Y. Zhang, W. Zhao, N. E. Zhang, Y. J. Zheng, S. Elshahat, Y. C. Liu. On-chip topological nanophotonic devices. *Chip*. **1**, 100025 (2022). <https://doi.org/10.1016/j.chip.2022.100025>.
 27. Z. N. Tian, F. Yu, X. L. Zhang, K. M. Lau, L. C. Wang, J. S. Li, C.T. Chan, Q. D. Chen. On-chip single-photon chirality encircling exceptional points. *Chip*. **1**, 100066(2023). <https://doi.org/10.1016/j.chip.2023.100066>.
 28. R. Streubel, S. Barcikowski, B. Gökce. Continuous multigram nanoparticle synthesis by high-power, high-repetition-rate ultrafast laser ablation in liquids. *Opt. Lett.* **41**, 1486–1489(2016). <https://doi.org/10.1364/OL.41.001486>.
 29. F. Raza, I. Ahmed, H. Ullah, W. Hammad-ul, U. Khan and Y. P. Zhang. Multi-channel router and logic NAND gate from multiple Autler-Townes splitting controlled by phase transition. *RSC ADVANCES*. **10**(16), 15239–15244(2020).<https://doi.org/10.1039/D0RA01379J>.
 30. B. Romero, S. Bruque, M. A. G. Aranda and J. E. Iglesias, Syntheses. Crystal Structure, and Characterization of Bismuth Phosphates. *Inorg. Chem*, **33**, 1869–1874(1994). <https://doi.org/10.1002/chin.199436005>.
 31. D. Serrano, S. Kuppasamy, B. Olaf Fuhr, D. Hunger, M. Ruben, and P. Goldner. Ultra-narrow optical linewidths in rare-earth molecular crystals. *Nature*. **603**, 241–246(2022). <https://doi.org/10.1038/s41586-021-04316-2>.
 32. T. Zhong, J. Kindem, J. Bartholomew, J. Rochman, I. Craiciu, E. Miyazono, M. Bettinelli, E. Cavalli, V. Verma and S. Nam, Nanophotonic Rare-earth Quantum Memory with Optically Controlled Retrieval. *Science*. **357**, 1392–1395(2017). <https://doi.org/10.1126/science.aan5959>.
 33. Y. Ma, Z. Zhou, C. Li and G. Guo. Onehour Coherent Optical Storage in an Atomic Frequency Comb Memory. *Nat. Commun.* **12**, 2381(2021). <https://doi.org/10.1038/s41467-021-22706-y>.
 34. R. C. L. Mooney-Slater. Polymorphic of Bismuth Phosphate. *Z. Kristallogr.* **117**, 371–385(1962). <https://doi.org/10.1524/zkri.1962.117.16.371>.
 35. J. Y. Li, J. F. Zhu, M. Imran, H. R. Fan, A. Mujahid, F. Nadeem, P. Li, and Y. P. Zhang. Superior atomic coherence time controlled by crystal phase transition and optical dressing. *Opt. Lett.* **47**(9), 2310–2313(2022). <https://doi.org/10.1364/OL.446322>.
 36. H. R. Fan, F. Raza, I. Ahmed, M. Imran, F. Nadeem, C. B. Li, P. Li and Y. P. Zhang. Photon-phonon atomic coherence interaction of non-linear signals in various phase transitions Eu³⁺: BiPO₄. *Nanomaterials*. **12**(23), 4304(2022). <https://doi.org/10.3390/nano12234304>.
 37. Y. Zhao, M. Imran, A. Mujahid, I. Ahmed, C. B. Li, F. Nadeem, and Y. P. Zhang. Temporal interaction of hybrid signals in various phases of Eu³⁺: BiPO₄ through photonphonon dressing. *New J. Phys.* **24**(8), 083037(2022). <https://doi.org/10.1088/1367-2630/ac88ed>.
 38. P. Li, F. Li, X.Y. Zhang, Y. M. Li, X. X. Luo, R. M. Wang, Y. Cai, and Y. P. Zhang. Orthogonally Polarized Luminescence of Single Bismuth Phosphate Microcrystal Doped with Europium. *Adv. Optical Mater.* **8**(17), 2000583 (2020). <https://doi.org/10.1002/adom.202000583>.
 39. P. Li, Y. X. Guo, A. Liu, X. Yue, T. L. Yuan, J. P. Zhu, Y.P. Zhang, and F. Li. Deterministic relation between optical polarization and lattice symmetry revealed in ion-doped single microcrystals. *ACS Nano*. **16**(6), 9535–9545(2022). <https://doi.org/10.1021/acsnano.2c02756>.

40. P. Li, Y. P. Zhang, L. Zhang, F. Li, Y. X. Guo, Y. H. Li, W. P. Gao. Phase control of Eu^{3+} -doped YPO_4 nano/microcrystals. *Cryst. Growth Des.* **17**(11), 5935-5944 (2017). <https://doi.org/10.1021/acs.cgd.7b01038>.
41. P. Li, T. L. Yuan, F. Li, and Y. P. Zhang. Phosphate ion-driven BiPO_4 : Eu phase transition. *J. Phys. Chem. C.* **123** (7), 4424-4432 (2019).
- <https://doi.org/10.1021/acs.jpcc.8b10410>.
42. Y. S. Liu, D. T. Tu, H. M. Zhu and X. Y. Chen. Lanthanide-doped luminescent nanoprobe: controlled synthesis, optical spectroscopy, and bioapplications. *Chem. Soc. Rev.* **42**, 6924-6958 (2013). <https://doi.org/10.1039/C3CS60060B>.

Declaration of interests

☒ The authors declare that they have no known competing financial interests or personal relationships that could have appeared to influence the work reported in this paper.

☐ The authors declare the following financial interests/personal relationships which may be considered as potential competing interests:

--